Dual-plane PIV technique to resolve complete velocity gradient tensor in a turbulent boundary layer

by

BharathramGanapathisubramani[(1)], Ellen K Longmire[(2)], Ivan Marusic[(3)]
Department of Aerospace Engineering and Mechanics, University of Minnesota
107 Akerman Hall, 110 Union Street SE, Minneapolis, MN 55455
E-mail : [(1)]bugs@aem.umn.edu, [(2)]ellen@aem.umn.edu, [(3)]marusic@aem.umn.edu
and
Stamatios Pothos
TSI Incorporated, 500 Cardigan Road, Shoreview, MN 55126
E-mail : stamatios.pothos@tsi.com

Abstract

Simultaneous dual-plane PIV experiments were performed in streamwise-spanwise planes in the log region of a turbulent boundary layer at a moderate Reynolds number ($Re_\tau \sim 1100$). The acquired datasets were used to resolve all 9 velocity gradients from which the complete vorticity vector and other invariant quantities like 3-D swirl strength were computed. These derived quantities were used to analyze and interpret the structural characteristics and features of the boundary layer. Sample results of the vorticity vector and the 2-D swirl strength from the two neighboring planes indicate the existence of hairpin shaped vortices inclined downstream along the streamwise direction. These vortices envelop low speed zones and generate Reynolds shear stress that enhances turbulence production. Plots of 3-D swirl strength indicate the existence of additional vortical structures in the middle of low speed zones that may represent heads of smaller eddies intersecting the measurement plane which is in accordance with the hierarchy of structure size in a hairpin packet proposed by Adrian *et al.* (2000). Two-point correlations computed using the PIV data reveal that instantaneous production ($uw(\partial U/\partial z)$) occurs in spatially compact regions ($\sim$ 75 wall-units in length) on either spanwise side of a hairpin core. Computation of inclination angles of individual eddies using the vorticity vector suggests that most cores are inclined at 25° to the streamwise-spanwise plane with a resulting projected eddy inclination of 32° in the streamwise-wall-normal plane.

1 Introduction

Over the past few decades, researchers have worked toward understanding the eddy structure within turbulent boundary layers in order to develop effective simplifying models. Recently, Adrian *et al.* (2000) have reinforced the viewpoint that "hairpin vortices" are a primary feature in turbulence transport and production. The authors performed PIV experiments in streamwise-wall-normal planes of a turbulent boundary layer and found instantaneous footprints of heads of hairpin vortices. Most significantly, they also observed that these vortices traveled together in groups, termed "hairpin packets". Recently, Ganapathisubramani *et al.* (2003), with stereoscopic PIV data in streamwise-spanwise planes, concluded that these hairpin packets occupy only a small percentage of the total area, but contribute to a significant proportion of the total Reynolds shear stress gen-

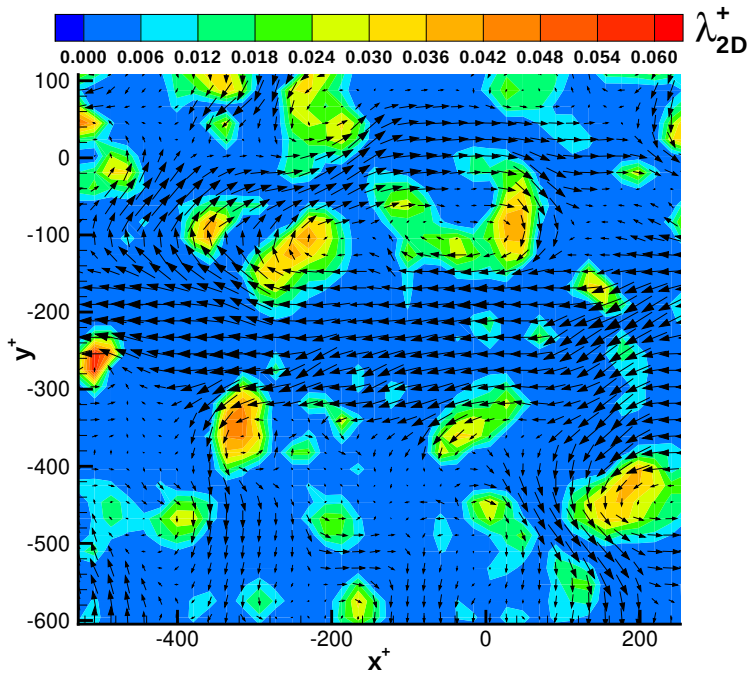

Figure 1: *Two-dimensional swirl strength (λ^+_{2D}) at $z^+ = 125$. The flow is from left to right. The vectors show in-plane velocity in convecting reference frame.*

erated, conservatively more than 30%. Hence, the hairpin packets are a very important mechanism in turbulence production. However, a detailed understanding of the three dimensional structure of hairpin vortices and packets is not yet available, and many questions regarding the shape, size, orientation and dynamics or these structures remain unanswered. Hence, the objective of the current experimental study is to obtain three dimensional data on velocity gradients in order to begin answering these questions.

To resolve the complete structure of a vortex, it is necessary to measure all three components of vorticity. With the single plane data obtained in most PIV experiments, the intensity or orientation of the vortices responsible for generation of Reynolds shear stress cannot be characterized completely. Specifically, the velocity gradients normal to the measurement plane are unknown. For example, Figure 1 illustrates swirl strength (λ_{2D}) calculated from the imaginary part of the eigenvalue of a 2-D velocity gradient tensor (based on in-plane gradients only. For reference see Zhou *et al.* (1999)). Although it performs reasonably well at identifying vortex core locations, it does not reveal the full swirl strength or the angle of the vortices. In the current study, dual-plane PIV datasets are used to retrieve the complete velocity gradient tensor.

2 Experiment and methods

Experiments were performed in a suction type boundary layer wind tunnel. Measurement planes were located 3.3 m downstream of a trip wire in a zero-pressure-gradient flow with freestream velocity $U_\infty = 5.9$ m s^{-1} and $Re_\tau = 1060$ ($Re_\tau = \delta U_\tau/\nu$, where δ is the boundary layer thickness, U_τ is the skin friction velocity). The streamwise, spanwise and wall-normal directions are along the x , y and

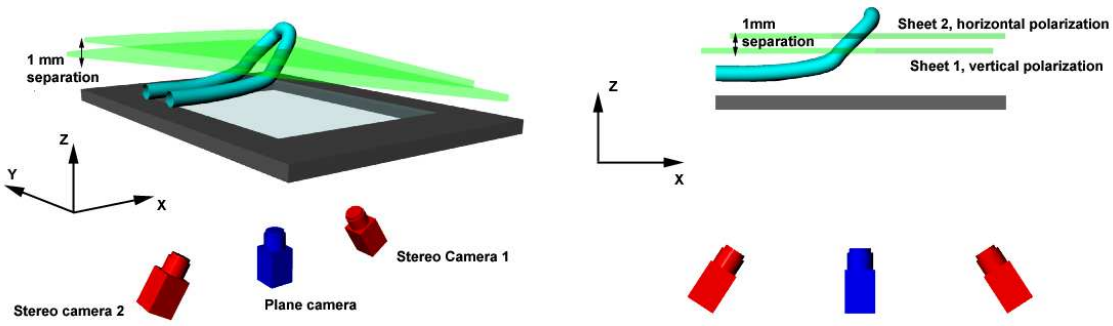

(a) (b)

Figure 2: *(a) Perspective view (b) side view of the experimental setup*

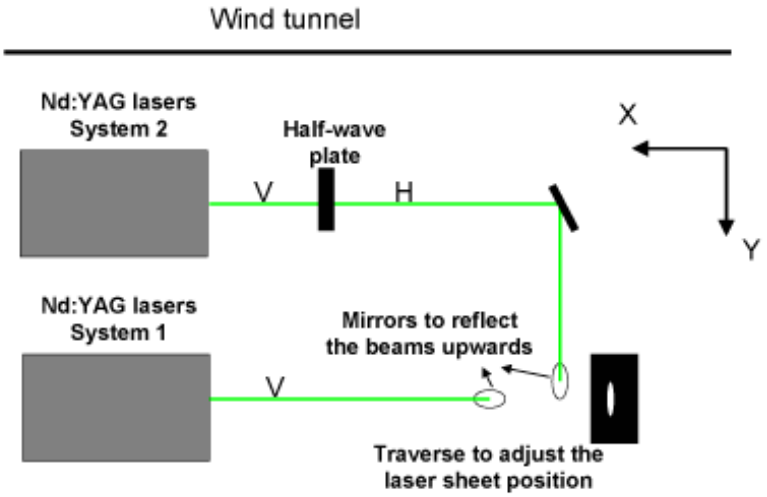

Figure 3: *Top view of laser setup. V and H designate the direction of vertical and horizontal polarization respectively.*

z axes respectively.

Two independent PIV systems capture data simultaneously in neighboring streamwise-spanwise planes separated by ~ 1 mm (15 wall units) as shown in figure 2. System 1 is a stereoscopic system used to provide all three velocity components over a plane illuminated by Sheet 1, and System 2 is a single-camera planar PIV system. The single-camera system measures the streamwise-spanwise velocity components in the higher plane illuminated by Sheet 2. Simultaneous measurements are performed utilizing the polarization property of the laser light sheets to isolate one plane to one set of camera/cameras (see e.g. Raffel *et al.* 1998, Hu *et al.* 2001 , Christensen & Adrian 2002). PIV data were captured in the log layer of the turbulent boundary layer at $z^+ = 125$ (System 1) and at $z^+ = 140$ (System 2).

System 1 includes two TSI Powerview $2k \times 2k$ pixel resolution cameras equipped with Nikon 50 mm lenses. The lenses are fitted with linear polarizers (two in series) oriented to allow the passage of vertically polarized light only. Light sheets are generated by a pair of Big Sky CFR-

200 series Nd:YAG lasers (120 mJ/pulse) that are vertically polarized. System 2 includes one TSI Powerview camera with $2k \times 2k$ pixel resolution and a Nikon 50 mm lens. The linear polarizers in this case are oriented to allow the passage of horizontally polarized light only. The illumination source for this setup is a pair of New Wave Nd:YAG lasers (120 mJ/pulse) with beams that are vertically polarized. A half wave plate (from CVI Laser) is used to rotate the polarization of the System 2 laser beams by 90 degrees as shown in figure 3. Each laser pair is aligned independently to illuminate a specific wall-normal location. The timing of each laser/camera system is controlled using a TSI synchronizer box. In order to ensure simultaneous capture of images, an external trigger is provided to both synchronizer boxes for image capture at a frequency of 0.2 Hz. The data from the two systems are streamed continuously to the hard drives of two Dell Precision workstations. Vector fields are computed using a 32×32 pixel window in both planes. The vectors from each camera in the stereo plane are then combined using suitable magnification factors to compute all three velocity components (see Ganapathisubramani *et al.* 2002). The vector field from the single camera is resampled and mapped to the grid of the stereo measurement using bi-linear interpolation. The resolution of the resulting vector fields is about 18×18 wall units, and the total field size is $1.8\delta \times 1.8\delta$.

The single camera vector field from the upper plane in liaison with the stereoscopic data from the lower plane are then used to compute all velocity gradients in the lower plane. A second order central difference method is used to compute all possible in-plane gradients while a first order forward difference is used to compute the wall-normal gradients of the streamwise and spanwise velocities. Finally, the continuity equation is used to recover the wall-normal gradient of the wall-normal velocity. With the out-of-plane gradients provided by the dual-plane data, we are able to compute the complete swirl strength and vorticity vector.

3 Uncertainty in computed gradients

A complete uncertainty analysis was performed to quantify the validity of the computed gradients. The uncertainty in any gradient is dependent on the differencing scheme used to compute it. A simple error propagation analysis was used to compute the uncertainties in the gradients at a single-point as described by Kline & McClintock (1953). For in-plane velocity gradients, the primary contribution to the uncertainty are from the pixel-resolution and stereoscopic reconstruction.

The uncertainty in sheet separation makes a significant contribution to the uncertainty in the gradient in the wall-normal direction. The absolute uncertainty in the gradient increases with uncertainty in sheet separation. In this experiment, the wall-normal separation Δz is fixed as 1 mm within 100 μm certainty. Table 1 lists the computed absolute uncertainty in all 9 gradients and values normalized by each r.m.s (root mean square) of the gradients. Typically, in the velocity fields presented, we are interested in gradients that are twice the r.m.s. values. Hence, the relative uncertainties in larger gradients are smaller.

Column 5 in Table 1 shows the uncertainty in the gradients relative to twice the r.m.s. It is clear from this column that the uncertainty of all in-plane gradients is exactly half the value in column 4. However, the uncertainty in the out-of-plane gradients of U and V is marginally higher than half the value in column 4. The uncertainty in sheet separation causes this difference. It is important to note that the uncertainties in the wall-normal gradients could be reduced considerably by reducing the uncertainty in measuring the sheet separation. Note also that the results in Table 1 reflect the

Table 1: *Uncertainties in velocity gradients. K is any gradient and δK is the uncertainty in the gradient.*

K	σ_K (s^{-1})	Absolute δK (s^{-1})	% $\frac{\delta K}{\sigma_K}$	% $\frac{\delta K}{2\sigma_K}$ (Typical)
$\frac{\partial U}{\partial x}$	49.49	6.87	14.02	7.01
$\frac{\partial U}{\partial y}$	79.21	6.87	8.5	4.25
$\frac{\partial U}{\partial z}$	111.53	20.31	18.2	10.4
$\frac{\partial V}{\partial x}$	60.52	12.03	19.87	9.94
$\frac{\partial V}{\partial y}$	55.64	12.03	21.6	10.8
$\frac{\partial V}{\partial z}$	107.55	20.11	18.7	12.74
$\frac{\partial W}{\partial x}$	93.86	34.38	36.6	18.3
$\frac{\partial W}{\partial y}$	106.89	34.38	32.16	16.08
$\frac{\partial W}{\partial z}$	57.97	13.85	23.89	11.95

findings of Westerweel (1994), where the author found that gradients can be computed with 10-20% accuracy, provided the velocity data is within 1-2% accuracy.

The validity of the dual-plane-stereo gradients can be further judged by computing the wall-normal gradient of mean streamwise velocity ($\partial\overline{U}/\partial z$). This value can be compared with the wall-normal gradient predicted by the log law:

$$\frac{\partial\overline{U}}{\partial z} = \frac{U_\tau}{\kappa z}$$

where, z is the wall normal location and $\kappa = 0.42$ is the universal log-law constant. For our wall-normal location, which is 0.01 m from the wall, and skin friction velocity of 0.17 ms^{-1}, the log-law predicts the gradient to be 40.47 s^{-1}. The measured average value from an ensemble of 100 images (with resolution of 100 $\times$ 100 vectors) is 36.78 s^{-1}. The error in the mean value of the gradient is thus 8.9 % which is within the expected uncertainty for this first order difference quantity.

4 Results and Discussion

Figures 4(a) and 4(b) show the streamwise velocity fluctuation (u) contours from the lower and the upper planes respectively. It is clear that the two planes are very well correlated. The streamwise velocity signature is very streaky consisting of low and high speed regions. We can zoom in on one of these regions (marked with a box in figure 4) to study individual eddy structures and their three dimensional properties.

The wall-normal (ω_z^+) and streamwise (ω_x^+) components of vorticity of the boxed region are shown in figures 5(a) and (b). As seen from figure 4, this region is centered on a low speed zone. The plot of ω_z shows that the top of the low speed region is enveloped by negative values and the bottom by positive values. Also, the vectors seem to indicate that these regions of vorticity contain swirling motions indicative of vortex cores. However, the vortices seen here are not merely wall-normal vortices. This point becomes clear from the ω_x^+ plot. The regions of positive ω_z^+ have predominantly positive ω_x^+, and regions of negative ω_z^+ have negative ω_x^+. The data thus suggest the presence of hairpin type vortices inclined at an angle with respect to the streamwise direction. Note, however,

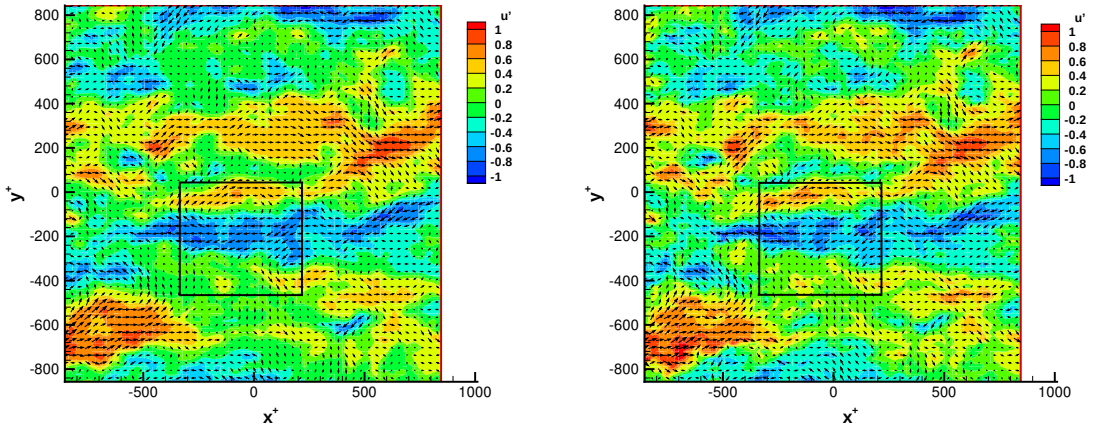

(a) (b)

Figure 4: *Fluctuating streamwise velocity (u) contours at (a)*$z^+ = 125$. $\overline{U}_1 = 3.34$ ms^{-1}, *(b)* $z^+ = 140$. $\overline{U}_2 = 3.38$ ms^{-1}.

that inclined hairpins are not the only type of instantaneous structures observed. Examination of various vector fields in the two neighboring planes indicate evidence of some structures that are inclined at 90 degrees to the streamwise direction and others that are completely streamwise.

To present further evidence that regions of strong vorticity correspond with vortex cores, we examine plots of the instantaneous swirl strength for the same boxed region shown in figure 4. Figure 5(c) reveals the instantaneous two dimensional swirl strength (λ_{2D}^+) at $z^+ = 125$. This plot in tandem with ω_z^+ (see figure 5(a)) shows that 2-D swirl isolates regions that are swirling about an axis aligned with the wall-normal direction. A visual comparison between the swirl in the lower and upper planes (not shown here) indicates a forward tilt to most structures as they are offset in the positive streamwise direction in the upper plane. (This trend is observable in many pairs of planes, in particular when they are viewed in rapid succession). However, if the inclination angles of vortices are large, λ_{2D}^+ does not do a good job at identifying them. Figure 5(d) presents a plot of the full swirl strength (λ_{3D}^+) that was computed utilizing the complete velocity gradient tensor. The plot reveals that the 3-D swirl identifies not only the hairpin shaped vortices cutting across the plane but also additional regions that are not isolated by 2-D (wall normal) swirl. Note for example the small light blue regions in the middle of the low speed zone (between the hairpin cores) that contain significant λ_{3D}^+ but not λ_{2D}^+. These regions could possibly coincide with smaller hairpin vortices whose heads are cutting across the measurement volume and hence are not apparent in the 2-D swirl plot.

Figure 6 is yet another example to illustrate the performance of λ_{3D}^+. It is clear from figures 6(a)-(c) that three dimensional swirl isolates a lot more than wall-normal vortices. Figure 6 also reveals a closer look into a region identified as a hairpin packet (outlined by the thick black line) by the algorithm described in Ganapathisubramani *et al.* (2003). Figure 6(d) shows instantaneous production, $uw^+(\partial U^+/\partial z^+)$. Some locations of strong production lie close to swirling zones. Previous work by Ganapathisubramani *et al.* (2003) indicated that regions of high Reynolds shear stress occurred within hairpin packets. Figure 6(d) shows high production levels in the packets near

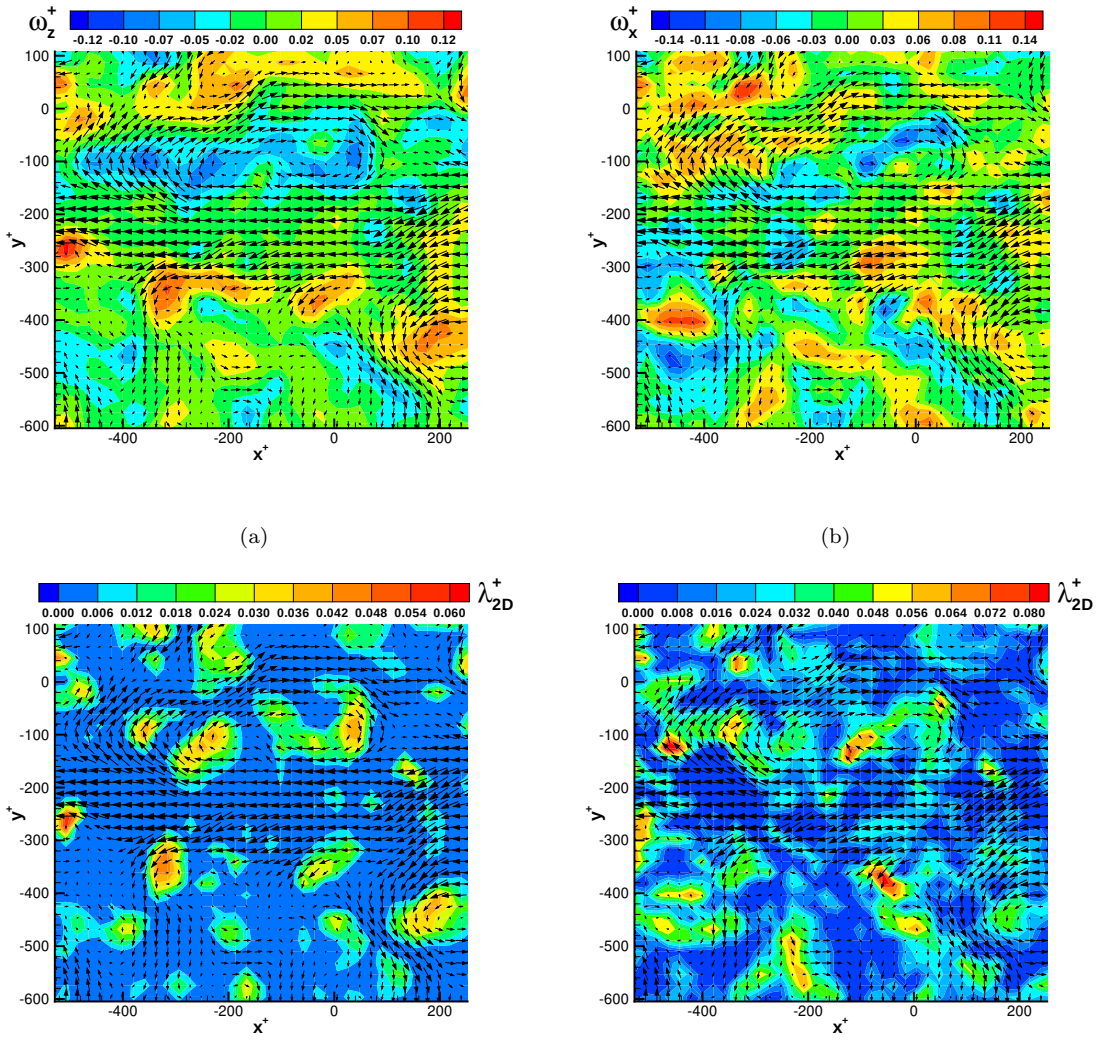

(a) (b)

(c) (d)

Figure 5: *Various quantities at* $z^+ = 125$ *(a)* ω_z^+*, (b)* ω_x^+*, (c)* λ_{2D}^+ *and (d)* λ_{3D}^+.

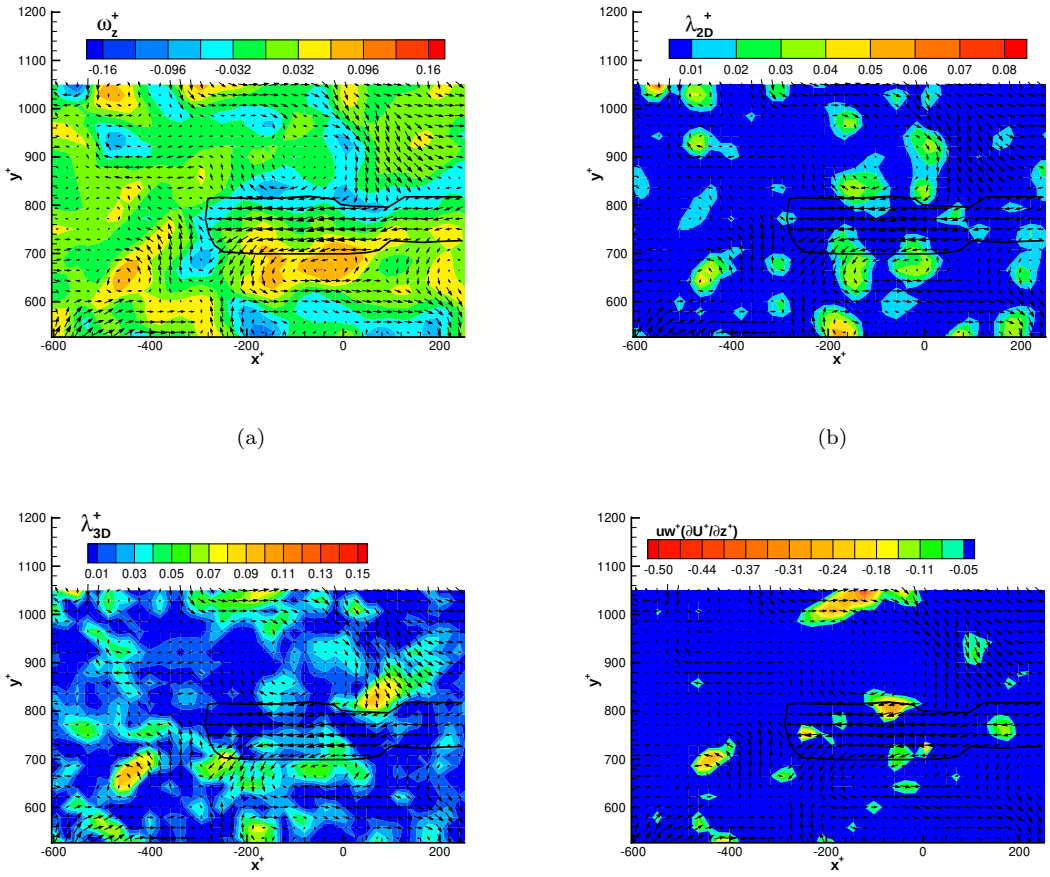

(a) (b)

(c) (d)

Figure 6: *Various quantities at* $z^+ = 125$. *(a)* ω_z^+, *(b)* λ_{2D}^+, *(c)* λ_{3D}^+ *and (d) Instantaneous production,* $uw^+ \frac{\partial U^+}{\partial z^+}$. *The dark line in the plots is the envelope of a low speed region identified as a hairpin packet by the algorithm described in Ganapathisubramani* et al. *(2003).*

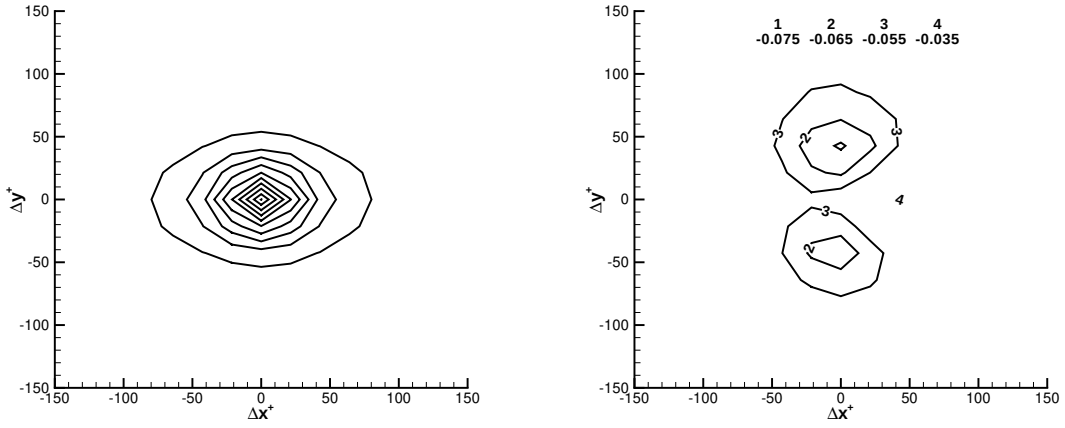

(a) (b)

Figure 7: *Two-point correlations. (a) Production auto correlation, contour levels range from 1.0 to 0.1 with 0.1 spacing, (b)λ_{2D}^+ and $uw^+(\partial U^+/\partial z^+)$ cross correlation, contour levels shown are labeled in the figure.*

the legs of hairpins. Other examples (not shown here) reveal strong Reynolds stress production in regions that lie close to zones of significant λ_{3D}^+ (but, no λ_{2D}^+) that could be heads or streamwise legs of hairpin structures.

Figure 7(a) shows the two-point auto-correlation of the production term at $z^+ = 125$. It is clear from the plot that turbulence production is spatially compact in both streamwise and spanwise directions. A characteristic length-scale for turbulence production in the streamwise direction of 75 wall-units can be inferred from this plot. The length-scale is smaller in the spanwise direction. The relationship between vortex cores and production can be further investigated by computing the two-point cross correlation between λ_{2D}^+ and $uw^+(\partial U^+/\partial z^+)$. Figure 7(b) reveals the contour plots of the aforementioned correlation. The plot reveals the extent of dependence between swirl strength and instantaneous production. Production seemingly occurs on either spanwise side of a vortex with significant wall-normal vorticity component which is analogous to turbulence production in both Q2 ($u < 0$, $w > 0$) and Q4 ($u > 0$, $w < 0$) regions. The two-point correlation between λ_{3D}^+ and $uw^+(\partial U^+/\partial z^+)$ does not have the two-lobed structure, which could be due to the presence of additional correlations from heads and streamwise legs of vortices. Note that these correlations were computed with a set of 100 images and hence the results are not well converged; however they are good enough to make qualitative conclusions.

The inclination angle of vortex structures can be computed by determining the orientation of the vorticity vector. If the vector angle is computed at every point in the field, the results are noisy because of both measurement uncertainty and the fact that instantaneous vortex lines in a turbulent flow are not very organized. By contrast, computation of the vorticity vector averaged over a region identified as a vortex core by the swirl strength λ_{3D}^+, leads to determination of the orientation of the vortex core. This orientation can then be interpreted as the local inclination of that vortex.

Figure 8(a) reveals the probability density function (p.d.f.) of the inclination angle (θ_e) vortex cores make with the $x - y$ plane. The angles were computed for all distinct regions of significant λ_{3D}^+. This distribution (square symbols) includes a wide range of structure angles at this wall-

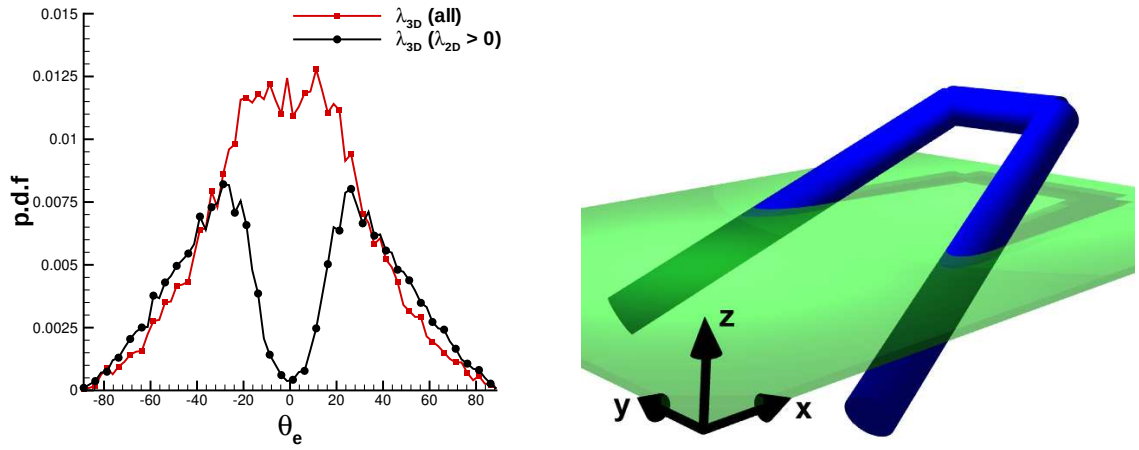

(a) (b)

Figure 8: *(a) p.d.f. of inclination angle (b) Schematic of hairpin structure*

normal location. Note that many structures have small inclination angles. Further study, including the investigation of the azimuthal angle made by the projection of the vorticity vector onto the $x-y$ plane with the x axis, reveals that most λ_{3D}^{+} regions with small inclinations are spanwise structures indicative of heads of smaller hairpin vortices. In order to obtain the inclination angles of cores that are not spanwise heads or streamwise legs, the average vorticity vector in isolated regions of λ_{3D}^{+} that includes λ_{2D}^{+} were computed. This additional criterion filters out spanwise and streamwise structures since λ_{2D}^{+} does not capture them. The resulting p.d.f., shown by circles in figure 8(a)) yields peaks at $\pm 25°$. This suggests that most cores are inclined at 25° to the $x-y$ plane. The angle made by the projection of the vorticity vector in the $x-z$ plane with the x axis is defined as the eddy inclination. The eddy inclination in the $x-z$ plane has a peak 32°. A schematic of a representative hairpin is shown in figure 8(b).

5 Conclusions

Simultaneous dual-plane PIV experiments were successfully performed to compute all nine velocity gradients in a turbulent boundary layer. Dual-plane measurements could be used to compute the complete vorticity vector and other quantities like instantaneous Reynolds shear stress production and 3-D swirl strength to study the eddy structure and their dynamics. Contours of different components of the vorticity vector and 2-D swirl strength from the two neighboring planes indicate the existence of hairpin shaped vortices inclined downstream along the streamwise direction. These vortices envelop the low speed zones and generate Reynolds shear stress that enhances turbulence production. Plots of 3-D swirl strength indicate the existence of additional vortical structures in the middle of low speed zones that may represent heads of smaller eddies intersecting the measurement plane. The dual-plane data could also be used in computation of typical vortex inclination angles at this wall-normal location. It is worth noting that this study includes just one dataset at one wall-normal location. Datasets at multiple wall-normal locations are required to resolve the complete vortex structure and learn more about the dynamics of a turbulent boundary layer.

Acknowledgements

The authors gratefully acknowledge support from the National Science Foundation through Grants ACI-9982274, CTS-9983933 and CTS-0324898, the Graduate school of University of Minnesota and the David and Lucile Packard Foundation. We are indebted to Dr. Nicholas Hutchins and William Hambleton for their help in data acquisition and many discussions during the course of this study.

References

Adrian, R. J., Meinhart, C. D., & Tomkins, C. D. 2000. "Vortex organization in the outer region of the turbulent boundary layer". *J. Fluid Mech.*, **422**, 1–53.

Christensen, K. T., & Adrian, R. J. 2002. "Measurement of instantaneous eulerian acceleration fields by particle image accelerometry: method and accuracy". *Exp. Fluids*, **33**, 759–769.

Ganapathisubramani, B., Longmire, E. K., & Marusic, I. 2002. "Investigation of three dimensionality in the near field of a round jet using stereo PIV". *J. Turbulence*, **3**, 017.

Ganapathisubramani, B., Longmire, E. K., & Marusic, I. 2003. "Characteristics of vortex packets in turbulent boundary layers". *J. Fluid Mech.*, **478**, 35–46.

Hu, H., Saga, T., Kobayashi, T., Taniguchi, N., & Yasuki, M. 2001. "Dual-plane stereoscopic particle image velocimetry: system set-up and its application on a lobed jet mixing flow". *Exp. Fluids*, **31**, 277–293.

Kline, S. J., & McClintock, F. A. 1953. "Describing uncertainties in single-sample experiments". *Mechanical Engineering*, **75**, 3–8.

Raffel, M., Willert, C., & Kompenhans, J. 1998. *Particle image velocimetry - A practical guide*. Springer-Verlag.

Westerweel, J. 1994. *Digital Particle Image Velocimetry - Theory and Applications*. Delft Unversity Press.

Zhou, J., Adrian, R. J., Balachandar, S., & Kendall, T. M. 1999. "Mechanisms for generating coherent packets of hairpin vortices in channel flow". *J. Fluid Mech.*, **387**, 353–396.